ZnO Rods with Exposed {100} Facets Grown via a Self-Catalyzed Vapor−Solid Mechanism and Their Photocatalytic and Gas Sensing Properties

Stella Vallejos,*,[†] Naděžda Pizúrová,[‡] Isabel Gràcia,[§] Carlos Sotelo-Vazquez,[∥] Jan Čechal,[⊥] Chris Blackman,[∥] Ivan Parkin,[∥] and Carles Cané[§]

[†]SIX Research Centre, Brno University of Technology, 10 Technická, 60190 Brno, Czech Republic

[‡]Institute of Physics of Material, Academy of Sciences of Czech Republic, 22 Zizkova, 61662 Brno, Czech Republic

[§]Instituto de Microelectrónica de Barcelona, Consejo Superior de Investigaciones Científica, Campus UAB, 08193 Bellaterra-Barcelona, Spain
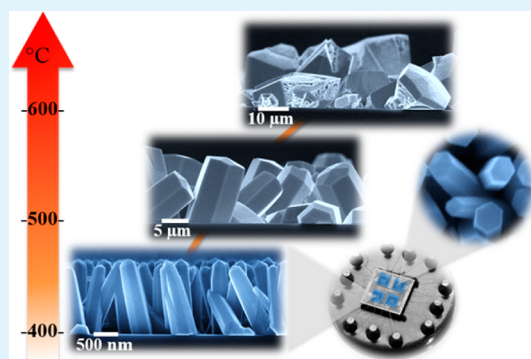
[∥]Department of Chemistry, University College London, 20 Gordon Street, London WC1H0AJ, U.K.

[⊥]Institute of Physical Engineering, Central European Institute of Technology, Brno University of Technology, 2896/2 Technická, 61669 Brno, Czech Republic

S *Supporting Information*

ABSTRACT: We present a new method for vapor deposition of columnar ZnO structures in the form of rods on various substrates without the need for substrate modification with catalyst seed particles and at relatively low temperatures compared to other vapor deposition methods. These structures are used for the photodegradation of stearic acid ($C_{18}H_{36}O_2$) and the photoactivated detection of gases such as carbon monoxide (CO), ethanol (C_2H_6O), toluene (C_7H_8), and nitrogen dioxide (NO_2) at room temperature, showing improved selectivity compared to tests performed in themoactivated mode.

KEYWORDS: *ZnO, rods, AACVD, gas sensing, photocatalysis*

INTRODUCTION

ZnO is a highly versatile wide direct band gap semiconductor with chemical, electrical, and optical properties that make it an ideal material for applications in optoelectronics, photovoltaics, energy generators, photocatalysis, and gas sensors, among others. Zinc oxide adopts a stable hexagonal wurtzite structure, and its morphological forms are generally dominated by nonpolar {100} and {110} and polar {00$\bar{1}$}, {001}, and {111} facets.[1−3] ZnO structures, e.g., in the form of rods, wires, and plates, etc., can lead to the formation of these specific facets and in turn to specific electronic structure at the surface. This has been found particularly important in surface-dependent applications such as photocatalyis and gas sensing, when attempting to tune the functionality of the material.[4−7] The first stage toward this morphological control requires synthetic methods capable of producing well-defined crystals, with uniform size, shape, and surface structure. New manufacturing strategies that are additive (bottom-up synthesis), rather than subtractive (top-down synthesis), are ideal for this task. Vapor-phase routes, for instance, are bottom-up approaches, industrially attractive, and potentially advantageous over liquid-phase routes, as they provide the ability to generate structured films in continuous rather than batch mode, with high purities and high throughput. Columnar ZnO structures in the form of rods or wires have been synthesized previously via vapor-phase routes although typically using pregrown catalyst seeds, i.e., via vapor−liquid−solid (VLS) mechanism, and/or high temperatures of 900−1300 °C;[2] which requires an extra surface pretreatment processing step and/or adds potential technological limitations for device fabrication.

Recently, however, we have recognized that aerosol-assisted chemical vapor deposition (AACVD) can lead to structured growth of metal oxides (MOX), e.g., WO$_3$[8] or SnO$_2$,[9] without the need for catalyst seeds, i.e., via vapor solid (VS) mechanism, and at relatively low temperatures.

AACVD is a variant of CVD that works at atmospheric pressure and relies on a solution-based delivery approach. This method is advantageous over traditional CVD as it allows for less volatile precursors to be utilized.[10] However, it also presents a number of challenges, including the selective

deposition of highly crystalline structures with well-controlled shapes avoiding agglomerates. To grow columnar structures via AACVD without the use of pregrown catalyst seeds requires precise control of the precursor/solvent supersaturation to prevent the formation of nonadherent powders or polycrystalline thin films. In this context, the choice of precursor/solvent and deposition conditions is crucial to ensure a degree of heterogeneous reaction on the substrate surface that promotes a compression of the nucleation rate parallel to the substrate and a decrease of the energy barrier for growth perpendicular to the substrate, a requirement determined previously for the formation of columnar WO_3 structures via AACVD.[11] A recent report on the AACVD of ZnO has also shown that the modification of a methanolic solution of $Zn(OAc)_2$ with acetic acid encouraged the growth of pyramidal microstructures perpendicular to the substrate without the need for substrate modification with catalyst seeds.[12] The AACVD of columnar ZnO structures in the form of rods, however, was achieved previously only at temperatures exceeding 550 °C by using pregrown TiO_2 catalyst seeds,[13] and to date no successful attempts to synthesize ZnO rods or wires without the use of catalyst seeds via AACVD have been reported, despite the natural tendency of the ZnO crystals grown via VS mechanism to form wurtzite wires with hexagonal cross-sections.[14]

Herein, we report the growth of ZnO rods via AACVD at 400 °C on various substrates, including silicon wafers, silicon-based micromachined platforms, and glass tiles, without the need for substrate pretreatment with catalyst seeds and their application in photocatalysis and gas sensing in photoactivated and thermoactivated mode

RESULTS AND DISCUSSION

AACVD of Zinc Oxide and Material Characterization. Generally the AACVD of $ZnCl_2$ on the Si substrates (10 mm × 10 mm × 0.5 mm) resulted in the formation of adherent uniform films of greyish color with good coverage of the substrate, except for the films synthesized at 600 °C, which showed reduced coverage and degraded structures (Figure S1, Supporting Information). ZnO in the form of rods was only obtained at 400 °C from a solution of $ZnCl_2$ and ethanol, showing no morphological changes as a function of the precursor concentration or substrate used.

SEM imaging of the rods (Figure 1) displayed a morphology characterized by a high density of quasi-aligned hexagonal-shaped rods with lengths of ~1600 nm and diameters of ~380 nm. XRD of these films (Figure 2a) revealed the presence of a hexagonal ZnO phase ($P6_3mc$ space group, a = 3.2490 Å, b = 3.2490 Å, and c = 5.2050 Å; ICCD Card No. 5-0664), with a high intensity peak at 34.34° 2θ (d = 2.60 Å) that indicate a strong preferred orientation in the [001] direction (similar XRD patterns were also present in the films grown from methanol- and acetone-based solutions). Measurements of the diffuse reflectance of these films indicated an optical bandgap at 3.2 ± 0.1 eV, consistent with the literature values for ZnO[4,5] (Figure S2, Supporting Information). Examination of the Zn 2p core level XPS spectra showed peaks at 1045 and 1022 eV corresponding to the Zn $2p_{1/2}$ and Zn $2p_{3/2}$ core levels, respectively, and a shakeup peak at 1040 eV (Figure 2b), consistent with those observed previously for ZnO.[15,16]

Estimation of the activation energy for the growth of the structures perpendicular (E_a^v) to the substrate indicated lower E_a^v when using ethanol-based solutions instead of acetone- or methanol-based solutions, whereas estimation of the activation
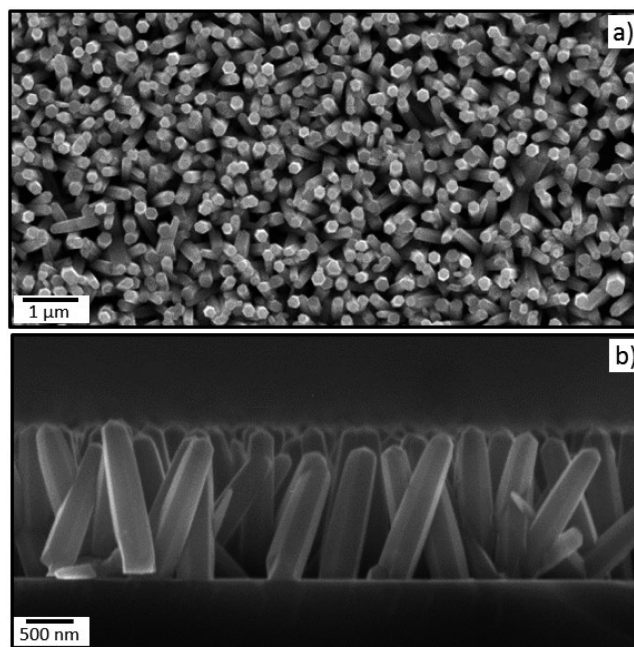

Figure 1. SEM images showing the top (a) and cross-sectional (b) views of the ZnO rods synthesized via AACVD.
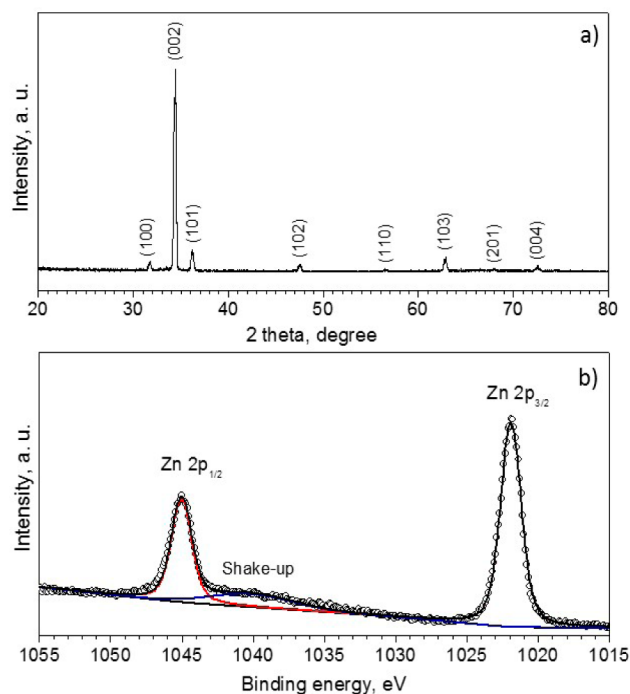

Figure 2. Typical XRD pattern (a) and Zn 2p core level XPS spectra (b) recorded on the ZnO rods.

energy for the growth parallel (E_a^h) to the substrate revealed higher E_a^h when using ethanol-based solution instead of acetone- or methanol-based solutions (Table 1). These results suggest that the incorporation of ethanol into the AACVD of $ZnCl_2$ increases the energy required for the interaction of the adatoms and the substrate surface (which inhibits the growth parallel to the substrate) and simultaneously reduces the energy needed for the adatom−adatom interaction (which favors the formation of columnar structures). The ratio of E_a^h to E_a^v for each system (0.8, 1.4, and 2.2 for methanol-, acetone-, and

Table 1. Activation Energy Estimated via Arrhenius Equation for the Perpendicular and Parallel Growth of the Films Synthesized from Methanol-, Acetone-, and Ethanol-Based Solutions

activation energy for the growth, kJ·mol^{-1}	for the given precursor solution		
	methanol	acetone	ethanol
E_a^v	55.9	58.8	43.1
E_a^h	46.3	83.9	95.8

ethanol-based solutions, respectively) indicates that the ZnO rods are grown via AACVD when E_a^h is more than twice E_a^v.

Previously we have noted that carrier solvents such as methanol and acetone can decompose at temperatures used for the AACVD of structures (<500 °C) leading to the formation of reactive intermediates, which become active species for deposition or react homogeneously to form solid particles.[8,17] However, this is not the case for ethanol, which forms reactive radical species at higher temperatures[18] than those used for the AACVD of ZnO rods. Hence, the higher ratio of E_a^h to E_a^v for the ethanol-based solution could be linked to a greater extent to the different physical properties of the solvent, particularly the surface tension, which alters the aerosol properties.[10] This difference in properties modifies the time needed for each solvent to transport the entire volume of solution (5 mL) and the flux $[\text{mol·(cm}^2\text{·s)}^{-1}]$ of precursor during the process; thus ethanol-based solution delivers the precursor at 50% and 67% lower rate than methanol- and acetone-based solutions, respectively.

Further analysis on the properties of the ZnO particles was achieved by EDX and TEM. EDX analysis of these particles confirmed the presence of Zn and revealed relatively low chlorine contamination (found for Cl:Zn 0.05 at. %), in line with those determined by XPS analysis (found for Cl:Zn of 0.08 (at. %), Figure S3, Supporting Information). Panels a and b of Figures 3 display the low magnification TEM image of a rod and its SAED pattern, respectively. This pattern is indexed to the $[\bar{1}10]$ zone axis of single-crystal hexagonal ZnO and demonstrates that the rods grown via AACVD are single-crystalline with growth in the $[001]$ direction. This is also evidenced by the marked planar spacing (0.26 nm) observed in HRTEM images (Figure 3c), which are consistent with the internal lattice of the (002) plane ($d = 0.26025$ nm) of the phase identified by XRD (Figure 2a). Similarly, the distance between atoms in the direction perpendicular to the growth revealed planar spacing of 0.16 nm, corresponding to the (110) crystallographic plane ($d = 0.16245$ nm) of the ZnO hexagonal phase. This orientation of the crystals indicates that the rods are bound by {100} facets. The {100} facets are usually exposed and dominant on the surface of ZnO structures in the form of rods, as they become the most stable facets due to their low surface energy (2.3 J m^{-2}) when the structure grows along the $[001]$ direction.[1,14] The facets forming the apex of the rod were not evident from the HRTEM images (Figure 3c); however considering the angle between the crystallographic planes, the apex is likely formed by {111} facets. Schematic models of an ideal crystal bound by {100} facets projected in the $[\bar{1}10]$ direction and a cut of it along the plain $(11\bar{1})$ are also displayed in Figure 3d,e, respectively, and consistent with the morphology of the ZnO rods. Based on the geometrical features of the rods, these results indicate that the {100} facets cover approximately 90% of the structured film surface formed via the AACVD of ZnCl$_2$ dissolved in ethanol.
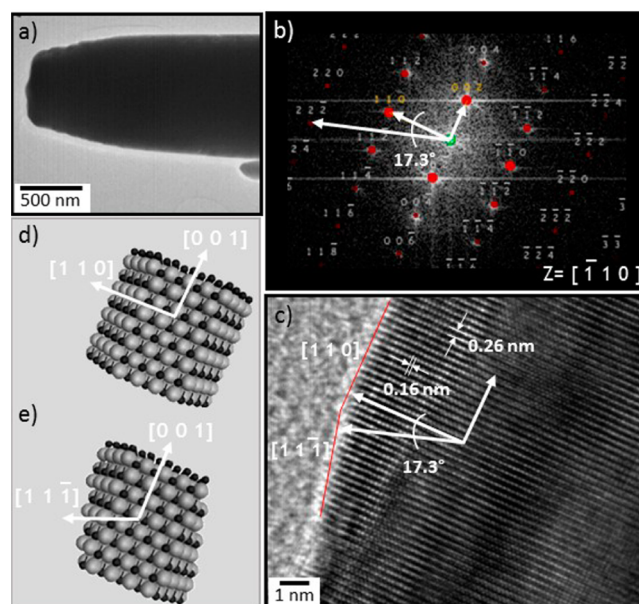

Figure 3. Typical low magnification TEM (a) of a ZnO rod particle and FFT pattern viewed along the $[\bar{1}10]$ direction (b). HRTEM (c) imaging of the particle, and schematic model of an ideal ZnO crystal viewed along the $[\bar{1}10]$ (d) and cut along the plain $(11\bar{1})$ in direction $[\bar{1}10]$ (e).

Photocatalysis. The photoactivity of the rods was evaluated by testing the degradation rate of stearic acid, a model organic pollutant.[19] To this end, rods were grown directly on glass substrates (10 mm × 10 mm × 1 mm) using the steps described above. The films displayed a whitish color with good coverage of the substrate. Examination of these samples showed identical morphology, crystal structure, and chemical composition as those observed for the structures grown on Si. The rate commonly expressed as the formal quantum efficiency (FQE), which estimates the number of acid molecules degraded per incident photon, indicated a 16-fold enhancement of the photoactivity for the ZnO rods compared to commercial photoactive glass (Pilkington, Activ) (Figure 4). This photoactivity is lower than those reported for other ZnO
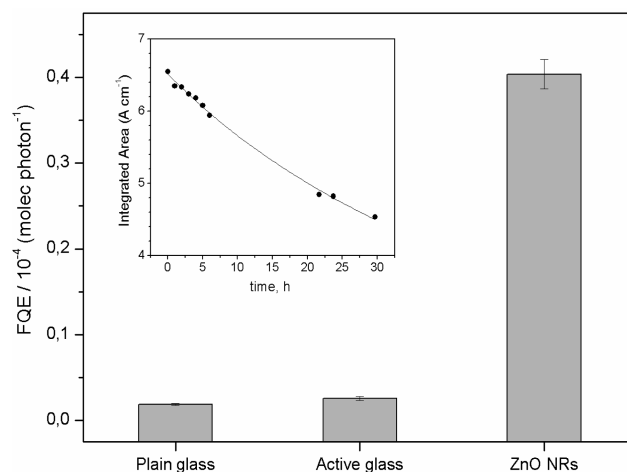

Figure 4. Formal quantum efficiencies, given as molecules degraded per incident phonon (molec·phonon^{-1}), and integrated area of the IR spectra (inset) obtained from the initial rates of photodegradation of stearic acid under UVA illumination (1.2 mW·cm^{-2}).

structures in literature,[20] which is likely related to the exposed {100} facets observed in the rods that have been shown to possess less photoactive sites compared, for instance, to the {001} facets.[4,5]

Gas Sensing. The gas sensing properties of the ZnO rods toward CO in a thermoactivated and photoactivated mode were also tested. To this end the rods were grown directly (without transfer of the structures) on micromachined platforms (1 mm × 1 mm × 0.01 mm) (Figure S4, Supporting Information). Analysis (SEM and XRD) of the ZnO grown onto the micromachined platform confirmed the integration of rods similar to those analyzed on Si and glass substrates. Photoactivated and thermoactivated gas sensing tests were carried out by monitoring the resistance changes of the film when exposing to 100 ppm of CO. The whole testing period comprised 4 weeks during which the microsensors were alternatively tested under different conditions accumulating a total of 140 h of operation. Comparison of the response in the first and fourth quarters of the testing period showed little dispersion of the results, demonstrating a good reproducibility of the response and stability of the sensitive material. Thermoactivated results showed sensor responses (S_R) for temperatures exceeding 125 °C, with the highest values registered at 305 °C (S_R = 200%), whereas photoactivated results demonstrated sensor responses at room temperature (RT) with faster rates of response to CO (r = 10) and greater resistance changes (S_R = 90%) than those observed in the thermoactivated test (r = 1.6 and S_R = 48%) at 250 °C (Figure 5 and Figure 6), which is consistent with that reported for other
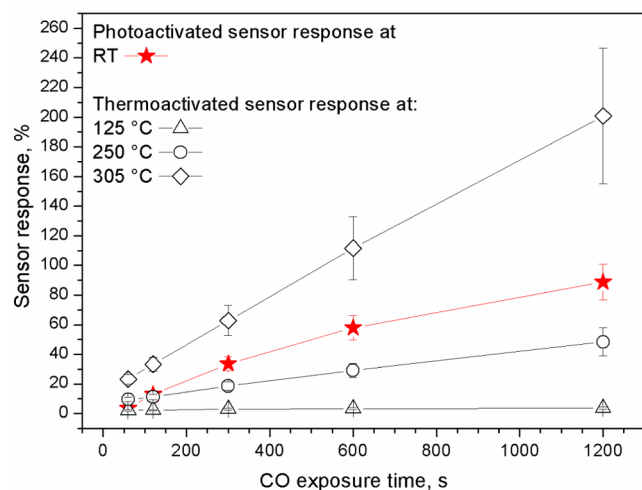

Figure 6. Rate of response to 100 ppm of CO obtained from the photoactivated tests performed at RT and thermoactivated tests at various sensor operating temperatures. The rate of response was estimated by fitting the change of resistance curve after CO injection to a logistic function, which was derived to obtain the rate law described by $-R/dt = rR^n$ (where r is the rate constant).

the lack of reversibility of the system at this temperature), and an increasing profile at 250 and 305 °C (associated with the long-time constants to stabilize the diffusion of oxygen atoms into the bulk of the material, a process that acts as a doping level modifier for the material affecting the total current density across the material for this range of temperatures)[22] (Figure S5, Supporting Information).

In order to evaluate the selectivity of the microsensors, further tests were performed to 100 ppm C_2H_6O, C_7H_8 (reducing analytes), and NO_2 (oxidizing analyte) both in photoactivated and thermoactivated modes. The analysis of variance of those responses (for a data set comprising four replicates of each analyte using four microsensors) is displayed in Figure 7. These results demonstrate low crossed-responses among the reducing analytes for the photoactivated tests (Figure 7a), as opposed to the thermoactivated tests which show noticeable overlaps of the response to CO, C_2H_6O, and C_7H_8 at 250 °C (Figure 7b) and CO and C_7H_8 at 305 °C (Figure S6, Supporting Information), suggesting an improvement of the selectivity when using the photoactivation.

The sensitivity of ZnO toward analytes such as CO, C_2H_6O, C_7H_8, and NO_2 was reported in the literature previously,[23−33] although only a few works described the correlation of the exposed facets with the sensor response in "real" devices, and often only to C_2H_6O. Generally, these works suggest that the {100} facets are the most stable surfaces in ZnO, providing long-term stability advantages to this sensitive material particularly when using thermoactivation,[1,26] but due to the presence of fewer dangling bonds in {100} facets, as opposed to other facets, e.g., {001} or {4$\overline{23}$}, the {100} facets have shown consistently less sensitivity.[23−26] The present work, however, has not experimentally proven gas sensing properties of other ZnO facets, and comparison of our results with the literature (Table 2) shows conflicting conclusions. For instance, the relative sensor response to parts per million concentration for our microsensors, based on {100} facets, toward C_2H_6O shows about 2 times higher values than those reported for {001} facets tested in photoactivated[25] or thermoactivated[23] mode. Other reports, in contrast, reveal opposite behavior, with our

Figure 5. Sensor response to 100 ppm of CO obtained from the photoactivated tests performed at RT and thermoactivated tests at various sensor operating temperatures.

MOX systems, when comparing their performance in thermoactivated and photoactivated mode.[21] Additionally, the changes in concentration (C) of CO showed typical power law fitting curves described as S_R = 0.27$C^{0.45}$ (photoactivated mode) and S_R = 1.32$C^{0.26}$ (thermoactivated mode) for the measured concentration levels from 25 to 100 ppm and from 5 to 100 ppm, respectively.

The ZnO rods also displayed better stability of the baseline resistance in the photoactivated mode, compared to the thermoactivated mode which led to a drift of the baseline resistance with a decreasing profile at 125 °C (associated with
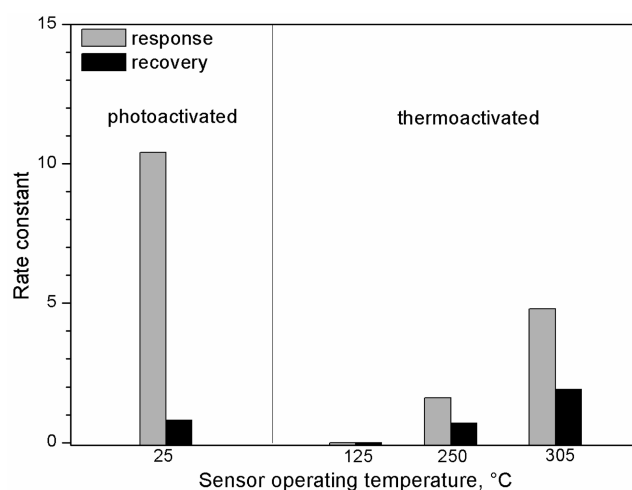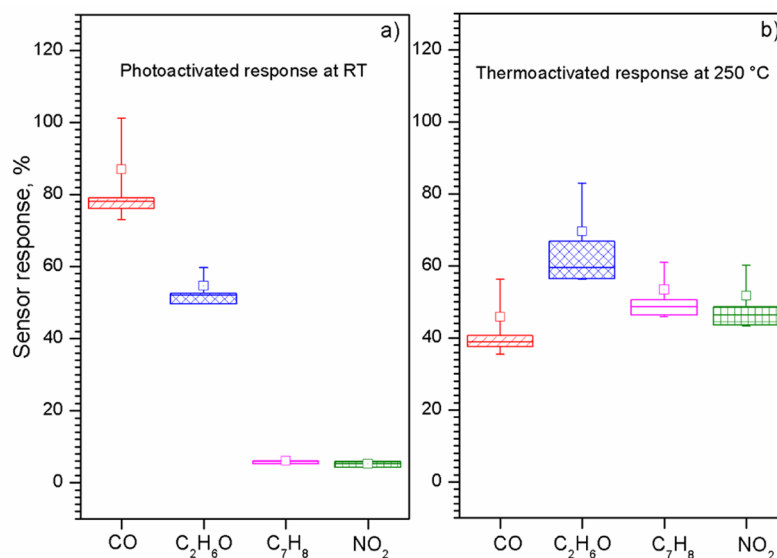
Figure 7. Box plots of the sensor response to 100 ppm CO, C_2H_6O, C_7H_8, and NO_2 obtained from the photoactivated tests at RT (a) and thermoactivated tests at 250 °C (b). Each box displays the median, mean, and upper and lower quartiles (first and third) of the respective distribution. Box whiskers indicate the standard error.

Table 2. Comparative Table Showing the Relative Sensor Response to Parts per Million Concentration (S_R/C) for the {100} AACVD Deposited ZnO Rods and Literature Reports for {001} and {4$\overline{2}\overline{3}$} ZnO Surfaces toward C_2H_6O[a]

exposed facets	S_R/C, %	T, °C	S_R	C, ppm	operation mode	ref
{100}	1.6	RT	1.6	100	photoactivated	this work
{001}	0.7	RT	1.3	200	photoactivated	25
{001}	5.5	305	5.5	100	thermoactivated	this work
{001}	10	300	20	200	thermoactivated	25
{001}	2.9	400	8.8	300	thermoactivated	23
{001}	174	330	87	50	thermoactivated	24
{4$\overline{2}\overline{3}$}	6.3	300	6.3	100	thermoactivated	26

[a]Data are based on the maximum response for closely similar operating temperatures and concentrations reported in each work. For comparison purposes the response was defined as R_a/R_g, where R_a and R_g represent the resistance in air and C_2H_6O, respectively.

microsensors showing almost 2[25] or 32[24] times lower responses than those recorded for thermoactivated {001} facets, or a response nearly similar to that reported for {4$\overline{2}\overline{3}$} facets (a more reactive surface compared to {100} or {001} surfaces).[26] A similar comparison with other ZnO morphologies including films,[27,29] particles,[30] wires,[28,34] or comb-like structures[31] (with no references to their dominant exposed facets) indicates improved photo- and thermoactivated responses for our microsensors toward C_2H_6O and CO (Figures S7 and S8, Supporting Information). Consequently, it is complex to attribute any improvement exclusively to the dominant exposed facets, as the fabrication and test conditions used in each work also impact the sensor performance; particularly the direct integration of structures into the device via AACVD (as opposed to most of the cited works which rely on transfer methods to integrate the sensitive material) provides cleaner surfaces that could favor the gas sensing properties of the ZnO rods.

The conductivity changes at RT in the photoactivated sensors toward reducing gases, such as CO, are connected with a previously recognized mechanism for nonphotoactivated MOX sensors, which involves the increment of the carrier concentration in the MOX due to the release of electrons in the conduction band when reactive gases combine with the preadsorbed oxygen ions at the MOX surface.[35] The nature of the preadsorbed oxygen, however, marks the differences in the sensing mechanism of the sensors photoactivated at RT, nonphotoactivated at RT, or thermoactivated above 150 °C (Figure 8). This is associated with the fact that at RT the photoactivation of ZnO leads to the formation of photoinduced O^-_{hv} and $O_2^-{}_{hv}$ species due the presence of excitons (Figure 8a), with the former being most likely dominant according to previous studies[25,36] (the presence of these photoinduced species at the surface of n-type semiconductors, such as ZnO, have been shown to decrease the baseline resistance of the sensitive material,[36,37] and this is consistent with the drop of resistance of ∼44% recorded after the photoactivation in air for the AACVD deposited ZnO structures). These photoinduced species make the ZnO surface chemically more active than that of a nonphotoactivated surface (Figure 8b), dominated by molecular O_2^- species[35] which are difficult to remove at RT. Then, it is the photoinduced oxygen species that participate in the oxidation/reduction of the analyte, and this explains the higher gas sensitivity at RT in the photoactivated mode. At temperatures above 150 °C, in contrast, the dominant species at the surface involve chemically active O^- and O^{2-} species with likely a higher density of O^{2-} species as the temperature increases,[35] which doubles the surface charge region in the preadsorption cycle (Figure 8c) and in turn results in a higher change of the conduction channel width (Figure 8f) compared to the nonphotoactivated (Figure 8e) and photoactivated (Figure 8d) modes at RT when a reducing gas such as CO is introduced. This is consistent with the higher responses recorded for the thermoactivated ZnO structures above 250 °C.

In summary, AACVD has been tuned for the seedless growth of ZnO rods with exposed {100} facets and has been used to grow these columnar structures directly on glass, silicon, or a
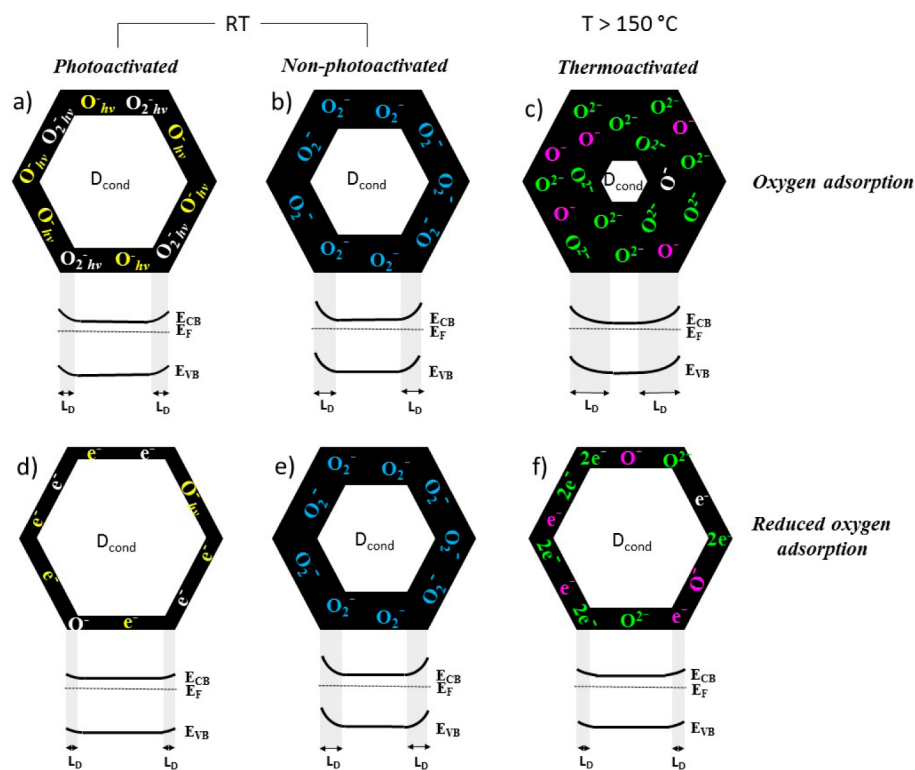
Figure 8. Schematic view of the cross-section of a rod showing the possible mechanism involved in the photoactivated (a, d), nonphotoactivated (b, e), and thermoactivated (c, f) detection of reducing analytes, such as CO or C_2H_6O, at the ZnO surface. D_{cond} represents the diameter of the nondepleted region available for charge conduction through the structure, E_{CB} the conduction band minimum, E_F the Fermi level, E_{VB} the valence band maximum, and L_D the Debye length or depth of the depletion region from the surface (not to scale).

silicon-based micromachined platform. Test of the photo-activity and gas sensitivity of these structures showed promising results, particularly for their sensing properties at RT by photoactivation. This characteristic becomes significantly advantageous in gas sensing, as it would allow for the sensor to operate without integrated heaters minimizing the power consumption of the system.

CONCLUSIONS

Columnar ZnO structures in the form of rods with exposed {100} facets have been vapor deposited via AACVD on various substrates, including silicon, glass, and micromachined platforms, without using catalyst seed particles (i.e., via VS mechanism) and at relatively low temperature (400 °C) compared to other CVD methods. The formation of rods was achieved when using an ethanol-based solution for the aerosol generation, which allowed for a 2-fold increase of the activation energy for the growth horizontal to the substrate, with respect to the activation energy for the growth parallel to the substrate. These columnar ZnO structures showed 16-fold higher photoactivity than commercial photoactive glass, and their photoactivated gas sensing properties at room temperature demonstrated the detection of reducing gases, such as CO and C_2H_6O, with improved selectivity than that obtained in the thermoactivated tests.

EXPERIMENTAL SECTION

AACVD of Zinc Oxide. ZnO films were synthesized from $ZnCl_2$ (Sigma-Aldrich, ≥98%) employing the AACVD system described previously.[38] Several conditions were probed including the use of various temperatures (from 300 to 600 °C), carrier solvents (either ethanol (Penta, ≥96%), acetone (Penta, ≥99.5%), or methanol (Penta,

≥99.8%)) and precursor concentrations (73, 55, or 40 mM). Also various substrates were employed, including silicon wafers, silicon-based micromachined platforms, and glass tiles, all without substrate pretreatment.

Material Analysis. The morphology of the films was examined using scanning electron microscopy (SEM; Tescan FE Mira II LMU), the phase using X-ray diffraction (XRD; Rigaku SmartLab 3 kW, Cu Kα radiation), and the chemical composition using X-ray photoelectron spectroscopy (XPS; Kratos Axis Supra with monochromatic Kα radiation, 300 W emission power, magnetic lens, and charge compensation on; the survey and detailed spectra were measured using pass energies of 160 and 20 eV, respectively). Further analysis of the material was carried out using transmission electron microscopy (TEM − JEM 2100F operated at 200 kV using a Schottky cathode and equipped with EDX). Selected area electron diffraction (SAED) and FFT patterns were validated using JEMS software, and HRTEM images were evaluated using Gatan Digital Micrograph software. TEM samples were prepared by removing the film from the substrates and depositing the suspended particles in ethanol onto Cu grids coated with carbon film.

Photocatalytic Tests. Prior to testing the photoactivity of the rods, the surface was UV-cleaned for 24 h under wet air using a UVA lamp (BLB lamp, 1.2 mW/cm^2). A Fourier transform infrared spectrometer (FTIR; PerkinElmer RX-I) was used to monitor the degradation of stearic acid. The samples were tested several times, and the degradation rates and quantum efficiency (FQE) data averaged as reported previously.[39]

Gas Sensing Tests. The silicon-based micromachined platforms were fabricated by micro-electromechanical systems (MEMS) technology and consisted of a suspended membrane, containing resistive heaters and interdigitated electrodes insulated by an interlevel silicon oxide layer.[9] The ZnO rods were integrated directly via AACVD on top of the electrodes using a shadow mask to confine the film deposition to the membrane and protect the contacts. Subsequently the chips were mounted and bound on a TO-8 package

as observed in Figure S4. These microsensors were tested in a continuous flow ($50 \, cm^3(STP)\cdot min^{-1}$) test chamber ($10 \, cm^3$ volume), provided with mass flow controllers, as described previously,[38] and continuous illumination from a lamp with wavelength of 147 nm (CDL 1021-0X, Analytical Control Instruments). The sensors were exposed to various concentrations of carbon monoxide (CO, Praxair), ethanol (C_2H_6O, Praxair), toluene (C_7H_8, Praxair), or nitrogen dioxide (NO_2, Praxair) during 60, 120, 240, 600, or 1200 s, and subsequently the gaseous analytes were purged with air (3X, Praxair) until the initial baseline resistance in air was recovered. The sensor response was defined as $[(R_a - R_g)/R_g]$ for the reducing analytes and $[(R_g - R_a)/R_a]$ for the oxidizing analyte, where R_a and R_g are the resistance in air and in gas, respectively.

ASSOCIATED CONTENT

Ⓢ Supporting Information

The Supporting Information is available free of charge on the ACS Publications website at DOI: 10.1021/acsami.6b12992.

> ZnO morphologies using different temperatures and solvents, diffuse reflectance spectra, survey XPS spectra, sensor device, film resistance changes to CO, box plots of the sensor response at 305 °C, and literature survey (PDF)

AUTHOR INFORMATION

Corresponding Author

*Tel.: +420 541 146 153. Fax: +420 541 146 2198. E-mail: vargas@feec.vutbr.cz.

ORCID Ⓘ

Stella Vallejos: 0000-0002-7415-5414

Notes

The authors declare no competing financial interest.

NOMENCLATURE

AACVD = aerosol-assisted chemical vapor deposition
C = concentration
E_a^h = activation energy for the growth parallel to the substrate
E_a^v = activation energy for the growth of the structures perpendicular to substrate
FQE = formal quantum efficiency
MOX = metal oxide
r = rate constant of sensor response
R_a = Sensor resistance in air
R_g = sensor resistance in target gas
S_R = sensor response
VLS = vapor–liquid–solid mechanism
VS = vapor–solid mechanism

REFERENCES

(1) Pal, J.; Pal, T. Faceted Metal and Metal Oxide Nanoparticles: Design, Fabrication and Catalysis. *Nanoscale* **2015**, 7, 14159–14190.

(2) Wang, Z. L. Splendid One-Dimensional Nanostructures of Zinc Oxide: A New Nanomaterial Family for Nanotechnology. *ACS Nano* **2008**, 2, 1987–1992.

(3) Cui, J. Zinc Oxide Nanowires. *Mater. Charact.* **2012**, 64, 43–52.

(4) McLaren, A.; Valdes-Solis, T.; Li, G.; Tsang, S. C. Shape and Size Effects of ZnO Nanocrystals on Photocatalytic Activity. *J. Am. Chem. Soc.* **2009**, 131, 12540–12541.

(5) Jang, E. S.; Won, J. H.; Hwang, S. J.; Choy, J. H. Fine Tuning of the Face Orientation of ZnO Crystals to Optimize Their Photocatalytic Activity. *Adv. Mater.* **2006**, 18, 3309–3312.

(6) Gurlo, A. Nanosensors: Towards Morphological Control of Gas Sensing Activity. SnO_2, In_2O_3, ZnO and WO_3 Case Studies. *Nanoscale* **2011**, 3, 154–165.

(7) Han, X.; Jin, M.; Xie, S.; Kuang, Q.; Jiang, Z.; Jiang, Y.; Xie, Z.; Zheng, L. Synthesis of Tin Dioxide Octahedral Nanoparticles with Exposed High-Energy {221} Facets and Enhanced Gas-Sensing Properties. *Angew. Chem.* **2009**, 121, 9344–9347.

(8) Vallejos, S.; Umek, P.; Blackman, C. Aacvd Control Parameters for Selective Deposition of Tungsten Oxide Nanostrucutres. *J. Nanosci. Nanotechnol.* **2011**, 11, 8214–8220.

(9) Vallejos, S.; Selina, S.; Annanouch, F. E.; Gracia, I.; Llobet, E.; Blackman, C. Aerosol Assisted Chemical Vapour Deposition of Gas Sensitive SnO_2 and Au-Functionalised SnO_2 Nanorods Via a Non-catalysed Vapour Solid (VS) Mechanism. *Sci. Rep.* **2016**, 6, 28464.

(10) Hou, X.; Choy, K. L. Processing and Applications of Aerosol-Assisted chemical Vapor Deposition. *Chem. Vap. Deposition* **2006**, 12, 583–596.

(11) Ling, M.; Blackman, C. Growth Mechanism of Planar or Nanorod Structured Tungsten Oxide Thin Films Deposited Via Aerosol Assisted Chemical Vapour Deposition (AACVD). *Phys. Status Solidi C* **2015**, 12, 869–877.

(12) Chen, S.; Wilson, R. M.; Binions, R. Synthesis of Highly Surface-Textured ZnO Thin Films by Aerosol Assisted Chemical Vapour Deposition. *J. Mater. Chem. A* **2015**, 3, 5794–5797.

(13) Sáenz-Trevizo, A.; Amézaga-Madrid, P.; Fuentes-Cobas, L.; Pizá-Ruiz, P.; Antúnez-Flores, W.; Ornelas-Gutiérrez, C.; Pérez-García, S. A.; Miki-Yoshida, M. Microstructural, Chemical and Textural Characterization of ZnO Nanorods Synthesized by Aerosol Assisted Chemical Vapor Deposition. *Mater. Charact.* **2014**, 98, 215–221.

(14) Vanmaekelbergh, D.; Van Vugt, L. K. ZnO Nanowire Lasers. *Nanoscale* **2011**, 3, 2783–2800.

(15) Gogurla, N.; Sinha, A. K.; Santra, S.; Manna, S.; Ray, S. K. Multifunctional Au-ZnO Plasmonic Nanostructures for Enhanced UV Photodetector and Room Temperature NO Sensing Devices. *Sci. Rep.* **2014**, 4, 6483.

(16) Sutka, A.; Timusk, M.; Dobelin, N.; Parna, R.; Visnapuu, M.; Joost, U.; Kaambre, T.; Kisand, V.; Saal, K.; Knite, M. A Straightforward and "Green" Solvothermal Synthesis of Al Doped Zinc Oxide Plasmonic Nanocrystals and Piezoresistive Elastomer Nanocomposite. *RSC Adv.* **2015**, 5, 63846–63852.

(17) Vallejos, S.; Di Maggio, F.; Shujah, T.; Blackman, C. Chemical Vapour Deposition of Gas Sensitive Metal Oxides. *Chemosensors* **2016**, 4 (1), 4.

(18) Park, J.; Zhu, R. S.; Lin, M. C. Thermal Decomposition of Ethanol. I. Ab Initio Molecular Orbital/Rice–Ramsperger–Kassel–Marcus Prediction of Rate Constant and Product Branching Ratios. *J. Chem. Phys.* **2002**, 117, 3224–3231.

(19) Mills, A.; Wang, J. Simultaneous Monitoring of the Destruction of Stearic Acid and Generation of Carbon Dioxide by Self-Cleaning Semiconductor Photocatalytic Films. *J. Photochem. Photobiol., A* **2006**, 182, 181–186.

(20) Kenanakis, G.; Giannakoudakis, Z.; Vernardou, D.; Savvakis, C.; Katsarakis, N. Photocatalytic Degradation of Stearic Acid by ZnO Thin Films and Nanostructures Deposited by Different Chemical Routes. *Catal. Today* **2010**, 151, 34–38.

(21) Prades, J. D.; Jimenez-Diaz, R.; Hernandez-Ramirez, F.; Barth, S.; Cirera, A.; Romano-Rodriguez, A.; Mathur, S.; Morante, J. R. Equivalence between Thermal and Room Temperature UV Light-Modulated Responses of Gas Sensors Based on Individual SnO_2 Nanowires. *Sens. Actuators, B* **2009**, *140*, 337−341.

(22) Malagù, C.; Giberti, A.; Morandi, S.; Aldao, C. M. Electrical and Spectroscopic Analysis in Nanostructured SnO_2: "Long-Term" Resistance Drift Is Due to in-Diffusion. *J. Appl. Phys.* **2011**, *110*, 093711.

(23) Liu, Y.; Dong, J.; Hesketh, P. J.; Liu, M. Synthesis and Gas Sensing Properties of ZnO Single Crystal Flakes. *J. Mater. Chem.* **2005**, *15*, 2316−2320.

(24) Qin, N.; Xiang, Q.; Zhao, H.; Zhang, J.; Xu, J. Evolution of ZnO Microstructures from Hexagonal Disk to Prismoid, Prism and Pyramid and Their Crystal Facet-Dependent Gas Sensing Properties. *CrystEngComm* **2014**, *16*, 7062−7073.

(25) Alenezi, M. R.; Alshammari, A. S.; Jayawardena, K. D. G. I.; Beliatis, M. J.; Henley, S. J.; Silva, S. R. P. Role of the Exposed Polar Facets in the Performance of Thermally and UV Activated ZnO Nanostructured Gas Sensors. *J. Phys. Chem. C* **2013**, *117*, 17850−17858.

(26) Su, D.; Fu, H.; Jiang, X.; Wang, G. ZnO Nanocrystals with a High Percentage of Exposed Reactive Facets for Enhanced Gas Sensing Performance. *Sens. Actuators, B* **2013**, *186*, 286−292.

(27) Hussain, M.; Mazhara, M.; Hussainb, T.; Khan, N. A. High Efficiency ZnO Nano Sensor, Fabrication and Characterization. *J. Iran. Chem. Soc.* **2010**, *7*, S59−S69.

(28) Zou, A. L.; Hu, L. Z.; Qiu, Y.; Cao, G. Y.; Yu, J. J.; Wang, L. N.; Zhang, H. Q.; Yin, B.; Xu, L. L. High Performance of 1-D ZnO Microwire with Curve-Side Hexagon as Ethanol Gas Sensor. *J. Mater. Sci.: Mater. Electron.* **2015**, *26*, 4908−4912.

(29) Pati, S.; Banerji, P.; Majumder, S. B. MOCVD Grown ZnO Thin Film Gas Sensors: Influence of Microstructure. *Sens. Actuators, A* **2014**, *213*, 52−58.

(30) Pati, S.; Maity, A.; Banerji, P.; Majumder, S. B. Qualitative and Quantitative Differentiation of Gases Using ZnO Thin Film Gas Sensors and Pattern Recognition Analysis. *Analyst* **2014**, *139*, 1796−1800.

(31) Zhang, H.-D.; Long, Y.-Z.; Li, Z.-J.; Sun, B. Fabrication of Comb-Like ZnO Nanostructures for Room-Temperature CO Gas Sensing Application. *Vacuum* **2014**, *101*, 113−117.

(32) Buchholz, M.; Yu, X.; Yang, C.; Heißler, S.; Nefedov, A.; Wang, Y.; Wöll, C. Ir-Spectroscopy of CO Adsorption on Mixed-Terminated ZnO Surfaces. *Surf. Sci.* **2016**, *652*, 247−252.

(33) Sin Tee, T.; Chun Hui, T.; Wu Yi, C.; Chi Chin, Y.; Umar, A. A.; Riski Titian, G.; Hock Beng, L.; Kok Sing, L.; Yahaya, M.; Salleh, M. M. Microwave-Assisted Hydrolysis Preparation of Highly Crystalline ZnO Nanorod Array for Room Temperature Photoluminescence-Based CO Gas Sensor. *Sens. Actuators, B* **2016**, *227*, 304−312.

(34) Hung, S. C.; Woon, W. Y.; Lan, S. M.; Ren, F.; Pearton, S. J. Characteristics of Carbon Monoxide Sensors Made by Polar and Nonpolar Zinc Oxide Nanowires Gated AlGaN/GaN High Electron Mobility Transistor. *Appl. Phys. Lett.* **2013**, *103*, 083506.

(35) Barsan, N.; Weimar, U. Conduction Model of Metal Oxide Gas Sensors. *J. Electroceram.* **2001**, *7*, 143−167.

(36) Li, W.; Xu, G. Unexpected Selectivity of UV Light Activated Metal-Oxide-Semiconductor Gas Sensors by Two Different Redox Processes. *J. Sens.* **2016**, *2016*, 1−6.

(37) Fan, S.-W.; Srivastava, A. K.; Dravid, V. P. UV-Activated Room-Temperature Gas Sensing Mechanism of Polycrystalline ZnO. *Appl. Phys. Lett.* **2009**, *95*, 142106.

(38) Vallejos, S.; Gràcia, I.; Figueras, E.; Cané, C. Nanoscale Heterostructures Based on $Fe_2O_3@WO_{3-x}$ Nanoneedles and Their Direct Integration into Flexible Transducing Platforms for Toluene Sensing. *ACS Appl. Mater. Interfaces* **2015**, *7*, 18638−18649.

(39) Quesada-Cabrera, R.; Sotelo-Vazquez, C.; Bear, J. C.; Darr, J. A.; Parkin, I. P. Photocatalytic Evidence of the Rutile-to-Anatase Electron Transfer in Titania. *Adv. Mater. Interfaces* **2014**, *1*, 1400069.